eNeuro

Research Article: New Research | Disorders of the Nervous System

Dysregulated mRNA Translation in the G2019S LRRK2 and LRRK2 Knock-Out Mouse Brains

https://doi.org/10.1523/ENEURO.0310-21.2021

Cite as: eNeuro 2021; 10.1523/ENEURO.0310-21.2021

Received: 20 July 2021
Revised: 4 October 2021
Accepted: 28 October 2021

1. Manuscript Title (50 words maximum):

Dysregulated mRNA translation in the G2019S LRRK2 and LRRK2 knockout mouse brains

2. Abbreviated Title (50 character maximum):

Dysregulated translation in the G2019S LRRK2 brain

3. List all Author Names and Affiliations in order as they would appear in the published article:

Author Names

Jungwoo Wren Kim[1,2,3], Xiling Yin[1,4], Ian Martin[1,4†], Yulan Xiong[1,4††], Stephen M. Eacker[1,4,5†††], Nicholas T. Ingolia[3], Ted M. Dawson[1,4,5,6,7,8 *] & Valina L. Dawson[1,2,4,5,6,8*]

Author Affiliations

[1]Neuroregeneration and Stem Cell Programs, Institute for Cell Engineering, Johns Hopkins University School of Medicine, Baltimore, MD 21205, USA.
[2]Department of Physiology, Johns Hopkins University School of Medicine, Baltimore, MD 21205, USA.
[3]Department of Molecular and Cell Biology, University of California, Berkeley, Berkeley, CA 94720, USA.
[4]Department of Neurology, Johns Hopkins University School of Medicine, Baltimore, MD 21205, USA.
[5]Adrienne Helis Malvin Medical Research Foundation, New Orleans, LA 70130, USA.
[6]Solomon H. Snyder Department of Neuroscience, Johns Hopkins University School of Medicine, Baltimore, MD 21205, USA.
[7]Department of Pharmacology and Molecular Sciences, Johns Hopkins University School of Medicine, Baltimore, MD 21205, USA.
[8]Diana Helis Henry Medical Research Foundation, New Orleans, LA 70130, USA.

4. Author Contributions:

J.W.K., V.L.D., and T.M.D. designed the study and wrote the manuscript; J.W.K. and I.M. performed biochemical experiments; J.W.K, S.M.E., and N.T.I. performed ribosome profiling and analyzed data; X.Y. performed Ca^{2+} imaging and Ca^{2+} current recordings; Y.X. generated transgenic mouse models.

5. Correspondence should be addressed to (include email address):

Valina L. Dawson or Ted M. Dawson
Neuroregeneration and Stem Cell Programs
Institute for Cell Engineering
Johns Hopkins University School of Medicine
733 North Broadway, Suite 731
Baltimore, MD 21205
Email: vdawson@jhmi.edu or tdawson@jhmi.edu

6. Number of Figures: 11 (5 Main, 6 Extended)

7. Number of Tables: 0

8. Number of Multimedia: 0

9. Number of words for Abstract: 223

10. Number of words for Significance Statement: 98

11. Number of words for Introduction: 207

12. Number of words for Discussion: 867

13. Acknowledgements:

Sequencing data were deposited to NCBI GEO: accession number GSE167704. T.M.D. is the Leonard and Madlyn Abramson Professor in Neurodegenerative Diseases. The authors acknowledge the joint participation by the Adrienne Helis Malvin Medical Research Foundation through its direct engagement in the continuous active conduct of medical research in conjunction with The Johns Hopkins Hospital and the Johns Hopkins University School of Medicine. The IRES reporters are gifts from P.A. Sharp's laboratory (Addgene #11509, #11510). [†]I.M's present address is Jungers Center for Neurosciences Research, Parkinson Center of Oregon, Department of Neurology, Oregon Health and Science University, Portland, OR 97239, USA. [††]Y.X's present address is Department of Neuroscience, University of Connecticut School of Medicine, Farmington, CT 06030, USA. [†††]S.M.E's present address is Phase Genomics Inc, Seattle, WA 98109, USA.

14. Conflict of Interest: Authors report no conflict of interest.

15. Funding sources:

This work was supported by grants from the NIH P50 NS38377, the JPB Foundation, and the Adrienne Helis Malvin Medical Research Foundation's Parkinson's Disease Program M-2014. J.W.K was supported by Korea Foundation of Advanced Studies. I.M. was supported by NIH/NIA grant K01-01AG050718. Y.X. was supported by NIH/NIA grant K01-AG046366 and The William N. & Bernice E. Bumpus Foundation Innovation Awards.

Dysregulated mRNA translation in the G2019S LRRK2 and LRRK2 knockout mouse brains

Abstract

The G2019S mutation in leucine-rich repeat kinase 2 (LRRK2) causes familial Parkinson's disease (PD) and is also found in a subset of idiopathic cases. Prior studies in Drosophila and human iPSC-derived dopamine neurons uncovered a pronounced effect of G2019S LRRK2 on mRNA translation. It was previously reported that G2019S LRRK2 promotes translation of mRNAs with complex 5' untranslated region (UTR) secondary structure, resulting in increased expression of calcium channels and dysregulated calcium homeostasis in human dopamine neurons. Here, we show that dysregulated translation occurs in the brains of mammalian LRRK2 models *in vivo*. Through ribosome profiling studies of global translation, we observe that mRNAs with complex 5'UTR structure are also preferentially translated in the G2019S LRRK2 expressing mouse brain. Reporter assays suggest that this 5'UTR preference is independent of translation initiation factors. Conversely, translation of mRNAs with complex 5'UTR secondary structure is downregulated in LRRK2 KO mouse brain, indicating a robust link between LRRK2 kinase activity and translation of mRNA with complex 5'UTR structure. Further, substantia nigra pars compacta (SNpc) dopamine neurons in the G2019S LRRK2 expressing brain exhibit increased calcium influx, which is consistent with the previous report from human dopamine neurons. These results collectively suggest that LRRK2 plays a mechanistic role in translational regulation, and the G2019S mutation in LRRK2 causes translational defects leading to calcium dysregulation in the mammalian brain.

Significance Statement

Parkinson's disease-linked G2019S mutation of LRRK2 is known to cause abnormalities in mRNA translation. These translational defects were suggested to cause calcium dysregulation, thereby imposing a long-term cellular stress to dopamine neurons. While these effects of G2019S LRRK2 on mRNA translation have been seen in Drosophila brain tissues and cultured mammalian neurons, translational profiling of the mammalian brain expressing G2019S LRRK2 has not been reported. In this study, we employed ribosome profiling to survey mRNA translation in the brains of LRRK2 mouse models, thereby demonstrating that the G2019S LRRK2 mutation broadly alters mRNA translation in the mouse brain.

Introduction

Dominant mutations in the leucine-rich repeat kinase 2 (LRRK2) gene are the most common genetic cause of familial Parkinson's disease (PD), with the G2019S missense mutation being most frequent disease-causing mutation in LRRK2 (Martin et al., 2014a). The G2019S mutation enhances the kinase activity of LRRK2, leading to neurotoxicity (Greggio et al., 2006; Smith et al., 2006). While various cellular functions are associated with LRRK2 kinase activity, emerging evidence suggests that alterations in mRNA translation downstream of kinase activity plays an important role in PD pathogenesis (Imai et al., 2008; Gehrke et al., 2010; Martin et al., 2014b; Taymans et al., 2015). G2019S LRRK2 was reported to increase global protein synthesis through phosphorylation of the ribosomal protein S15 (uS19), and reduction of global protein

synthesis is protective against G2019S LRRK2 neurotoxicity in a Drosophila model (Martin et al., 2014b). In addition, a recent study applying ribosome profiling to human dopamine neurons differentiated from patient-derived induced pluripotent stem cells (iPSCs) showed that the increased translation in G2019S LRRK2 leads to increased expression of genes responsible for calcium influx in neurons (Kim et al., 2020). While these studies presented potential mechanisms linking abnormal translation to cellular stress, the proposed mechanisms have yet to be tested in the mammalian brain.

Materials and Methods

All animal protocols are in accordance with the regulations of Johns Hopkins University Animal Care and Use Committee and the National Institutes of Health (NIH) *Guide for the Care and Use of Laboratory Animals.* Animals were housed in a 12-hour dark/light cycle with free access to water and food. High-throughput sequencing data is available via NCBI GEO (accession number: GSE167704).

Maintenance of LRRK2 transgenic mouse models

Generation and characterization of LRRK2 'Tet-off' transgenic mice and LRRK2 knockout mice were previously reported (Andres-Mateos et al., 2009; Nikonova et al., 2012; Xiong et al., 2017). For transgenic mice, high copy number lines (569 line for GS, 763 line for GS/DA) were used (Xiong et al., 2017). Single transgenic mice (CaMKII-tTA or Tet-LRRK2) were used for breeding, and the breeding cages were maintained with doxycycline chow (Diet-Sterile, 200 mg/kg doxycycline, Bio-Serv) and fed *ad libitum*. Doxycycline food was switched back to regular food after weaning for transgene

induction. 3 - 4 months old mice were used for ribosome profiling experiments (described below).

Mouse primary cortical neuron culture

Dissipated primary cortical neurons were prepared from E15 developing brain (CD1, Charles River or LRRK2 transgenic mice). Developing cortices were dissected in the dissecting medium (Dulbecco's Modified Eagle Medium (DMEM) with 20% horse serum, 0.5mM GlutaMax, 6μM glucose, Gibco), digested with TrypLE (Gibco), and plated at a concentration of 3×10^6 cells for a plate. Culture plates were pre-coated with 15μg/mL poly-L-ornithine. Cultures were maintained under Neurobasal (Gibco) medium with a serum-free supplement B-27 (Gibco) and 0.5mM GlutaMax (Gibco).

Immunocytochemistry of neurons

Cells were fixed with 4% paraformaldehyde for 15 minutes at room temperature, then permeabilized with 0.03% Triton X-100 for 15 min. The cells were washed then blocked for 1 hour with 10% goat serum in PBS. The blocked cells were subsequently incubated with primary antibody for overnight at 4°C. On the following day, the cells were incubated with secondary antibody for 1 hour at room temperature in a light controlled condition. After 3× wash with PBS buffer, the cells were mounted on cover slides with mounting media containing DAPI. All images were taken for analysis with Zeiss AxioObserver Z1 or LSM710 (Carl Zeiss) confocal laser scanning microscope under 20× or 40× oil objectives. Blinding was not performed with immunocytochemistry

experiments. The following primary antibodies were used for immunocytochemistry: α-TH (1:1000, EMD Millipore AB152).

Ribosome profiling library generation

Ribosome footprinting and RNA-seq libraries were prepared by following a published protocol with several modifications made for mouse brain tissue (Ingolia et al., 2012). Mouse brain: brains of 3-4 months old mice were dissected in TBS buffer with 100μg/mL cycloheximide, and immediately frozen in dry ice. Caudate putamen tissues from three mice of mixed gender (1:2 or 2:1 male:female ratio) were pooled. 2.5% of total lysate was subjected to western blotting to ensure sufficient expression of transgene. The collected samples were homogenized in lysis buffer (10mM Tris pH 7.5, 150mM NaCl, 5mM $MgCl_2$, 0.5mM DTT, 100μg/mL cycloheximide, EDTA-free protease inhibitor (Roche), 40U/mL murine RNase Inhibitor (NEB)) with 12 strokes of high-speed motorized homogenizer (Glas-Col GT series) at 40% power. The lysates were briefly centrifuged for 10 minutes at 2,000×g. The supernatant was transferred to a new tube, added NP-40 to 1% final concentration, incubated 5 minutes on ice. The samples were centrifuged again for 10 minutes at 20,000×g. The lysates were incubated in ice for 15 minutes, and centrifuged for 10 minutes at 20,000×g. Total RNA concentration of lysate was measured by Qubit RNA BR Assay (Life Technologies), and the same amount of RNA was used across samples. The supernatant was split into two tubes for ribosome footprinting and RNA-seq library generation.

Ribosome footprinting: The lysates were treated with 15μL of RNase I (Ambion) in 600μL total reaction volume for 45 min at room temperature, and the reaction was

198 stopped by adding 30μL of SuperAse-In (Ambion). Sucrose cushion was performed with
199 1.7g sucrose in 3.9mL polysome buffer (10mM Tris pH 7.5, 150mM NaCl, 5mM $MgCl_2$,
200 0.5mM DTT, 100μg/mL cycloheximide, 20U/mL SuperAse-In), 4 hours at 70,000rpm.
201 The pellet was resuspended with 700μL QIAzol (QIAGEN) reagent, incubated for 5
202 minutes at room temperature, 140μL chloroform was added, vortexed for 15 seconds,
203 and incubated again for 2 minutes at room temperature. The sample was centrifuged for
204 15 minutes at 12,000×g, the 350μL supernatant was mixed with 525μL 100% EtOH.
205 The mixture was loaded on an RNeasy Mini column (QIAGEN), and the RNA was
206 extracted. 26~34nt ribosome footprints were size-selected by Urea-PAGE, gel
207 extraction and RNA purification. Ribo-Zero Gold Kit (Illumina) was used for rRNA
208 removal after the size selection. The rRNA depleted ribosome footprints were
209 dephosphorylated by T4 polynucleotide kinase treatment, then Universal miRNA
210 Cloning Linker (NEB) was added to the 3' ends. Reverse transcription reaction was
211 performed, and the cDNA was circularized by CircLigase II (Epicentre) reaction, and
212 subjected to the PCR for final library generation.
213 RNA-seq: Total RNA was purified by a combination of QIAzol and RNeasy Mini as
214 described. Ribo-Zero Gold Kit was used for rRNA removal. RNA-seq library was
215 generated from the total RNA by ScriptSeq v2 Library Preparation Kit (Epicentre).
216
217 Ribosome profiling data processing
218 Illumina HiSeq 2000 or 2500 were used for deep sequencing of the libraries. FASTX-
219 Toolkit (http://hannonlab.cshl.edu/fastx_toolkit/) was used for the initial processing of the
220 reads.

Ribosome footprinting libraries: Only adapter-containing reads were clipped. Reads shorter than 25nt were discarded. The first nucleotide of the reads was trimmed. rRNA-mapped reads were discarded before genomic alignment.

RNA-seq libraries: Only adapter-containing reads were clipped, rRNA-mapped reads were discarded.

The processed reads were mapped to the UCSC genome database (mouse: mm9) by Tophat (2.0.11) with Bowtie2 (2.2.2). Maximum 1 mismatch was allowed for the alignments.

Sequencing read counts

Sample	Type	Mapped Reads
Mouse control 1	Ribo	11,528,964
	mRNA	35,167,826
Mouse control 2	Ribo	14,236,436
	mRNA	53,086,785
Mouse control 3	Ribo	28,913,143
	mRNA	37,446,599
G2019S TG 1	Ribo	10,832,574
	mRNA	37,329,310
G2019S TG 2	Ribo	11,636,313
	mRNA	42,813,645
G2019S/D1994A TG 1	Ribo	11,391,779
	mRNA	62,883,025

G2019S/D1994A TG 2	Ribo	30,967,177
	mRNA	33,887,256
Mouse WT (vs KO) 1	Ribo	6,069,632
	mRNA	44,668,380
Mouse WT (vs KO) 2	Ribo	6,331,204
	mRNA	8,025,070
LRRK2 KO 1	Ribo	5,552,451
	mRNA	65,571,861
LRRK2 KO 2	Ribo	7,322,616
	mRNA	18,455,674
LRRK2 WT 3 (STR)	Ribo	22,256,190
LRRK2 WT 3 (VMB)	Ribo	8,773,494
LRRK2 KO 3 (STR)	Ribo	22,069,910
LRRK2 KO 3 (VMB)	Ribo	6,492,191

Ribo: ribosome profiling, mRNA: RNA-Seq. TG: transgenic mice, WT: wild-type, KO: knockout mice. STR: striatum, VMB: ventral midbrain.

IRES reporter assays

pFR-HCV-xb, pFR-CrPV-xb vectors (from Phil Sharp Lab) were obtained from the Addgene depository (#11510, #11509, respectively). The reporter vectors were co-transfected into CD1 wild-type mouse cortical neurons at DIV 5 with LRRK2-expressing or S15-expressing plasmids (or empty, respective expression plasmids for control)

using Lipofectamine 2000 (Invitrogen) reagent. Luciferase to LRRK2/S15 expression vector ratio was 1:3. Culture medium was replaced (half-change) every 24 hours to minimize any potential effects from the growth condition including starvation. Luciferase activity was measured at DIV 7 by Dual-Glo Luciferase Assay System (Promega) (for the IRES reporters) with Glomax 20/20 Luminometer (Promega). The lysates were subjected to the total RNA purification with DNase treatment for the transcript level measurement.

Immunoblotting

Brain tissues were lysed with an automated homogenizer in RIPA buffer with 1% SDS (20mM Tris-HCl (pH 7.5), 150mM NaCl, 1mM EDTA, 1% NP-40, 1% sodium deoxycholate, 1% SDS, protease inhibitors). Lysates were incubated on a rotator for 1 hour at 4°C, and spun down for 10 min × 12,000g at 4°C. Supernatant was collected, protein concentration was measured, and the lysate was mixed with 2x Laemmli sample buffer. Generation and characterization of rabbit polyclonal T136 phospho-S15 antibody was previously published (Martin et al., 2014b). Commercial antibodies: LRRK2: Neuromab (75-188, N138/6); P-eIF2α (Cell Signaling Technologies, #9721); eIF2α (Cell Signaling Technologies, #9722); ATF4 (Millipore, ABE387).

Ribosome profiling data analysis

Aligned reads were counted by either a Python package HTSeq (htseq-count) or an R package GenomicAlignments (summerizeOverlaps). Annotations and sequencing reads were handled using an R package GenomicFeatures. To avoid multiple counting on

isoforms, transcript reference data were processed to have one unique annotation covering all isoforms (union of isoforms) per gene. Reads only in the CDS regions were counted. Transcripts with low read counts (<128 reads) were discarded. An R package DESeq (1.20) was used for calculating normalized expression from either ribosome footprinting or RNA-seq data based on a negative binomial distribution and generalized linear model. For the mouse data, replicates were initially analyzed independently to confirm reproducibility, and then analyzed in combination for the final analysis. For the human neuron data, biological triplicates were handled by DESeq. Translation efficiency was calculated based on the DESeq expression output. 5'UTR estimated folding energy table was extracted from the UCSC genome database (fold5UTR field: mm9). For the 5'UTR estimated folding energy comparison, a control group with similar group size was randomly selected for each comparison to avoid potential bias from sample size differences. Transcript coordinates were calculated by a custom R script and re-aligned based on the rounded half point of the ribosome footprint (5' end + (footprint length/2)). For icSHAPE data analysis, icSHAPE (*in vivo*) results from mouse ES cells (GEO: GSE64169) were downloaded, converted to mm9 (UCSC liftOver), and merged with our mouse ribosome profiling data.

Electrophysiological Recordings

Mice (10-12 weeks old) were anesthetized and decapitated, and the brains were placed in ice-cold artificial cerebrospinal fluid (ACSF) containing (in mM): NaCl 125, KCl 2.5, $MgSO_4$ 1, NaH_2PO_4 1.25, $NaHCO_3$ 26, $CaCl_2$ 2, and D-glucose 10. Transverse brain slices containing substantia nigra pars compacta (SNpc) (350 μm) were prepared using

a vibratome (Leica VT1200S). Sections were incubated in ACSF saturated with 95% O2 and 5% CO2, at 34°C for 60 min, and then at room temperature (22-24°C) until use. Recordings were performed at room temperature. All experiments were conducted in accordance with the National Institutes of Health guidelines for the care and use of animals.

HEKA EPC10 amplifier (HEKA Elektronik, Lambrech, Germany) was used to perform electrophysiological recordings. For spontaneous and evoked action potentials (APs), a single slice was transferred into a submerged recording chamber and perfused constantly with oxygenated ACSF at a rate of 2 ml/min. DA neurons were visualized under a 40× water immersion objective by fluorescence and DIC optics (Carl Zeiss, Germany). The patch electrodes had a resistance of 2–5 MΩ, and filled with solution containing (in mM): K-gluconate 126, KCl 8, HEPES 20, EGTA 0.2, NaCl 2, MgATP 3, Na_3GTP 0.5, Alexa Fluor 568 0.05 (pH 7.2, 290-300 mOsmol/kg). Input resistance (Rin), series resistance (Rseries), and leak currents (Leak) were monitored throughout the experiment. Unstable recordings (>10% fluctuation of Rseries value) during the course of experiments were rejected for further analysis. Resting membrane potential was recorded in current clamp mode at 0 pA immediately after establishing whole-cell configuration. A series of hyperpolarizing and depolarizing step currents were injected to elicit APs. For whole-cell calcium currents, the external solution used contained (in mM) tetraethylammonium methanesulfonate (TEA-$MeSO_3$) 140, HEPES 10, $BaCl_2$ or $CaCl_2$ 10 (pH 7.4, 300-310 mOsmol/kg). The pipette solution contained (in mM) $CsMeSO_3$ 135, CsCl 5, $MgCl_2$ 1, MgATP 4, HEPES 5, EGTA 5 (pH 7.3, 290-300 mOsmol/kg). Currents were recorded by holding the cell at –90 mV, before stepping to

various potentials from –60 mV to +50 mV for 250-ms in 10-mV increments. Tetrodotoxin (TTX, 1 μM) was used to block voltage-gated sodium currents. Data were acquired by PatchMaster software (HEKA Elektronik, Lambrech, Germany), sampled at 10 kHz, and filtered at 2.9 kHz. APs and calcium currents were analyzed using Clampfit 10.5 software (Molecular devices, Palo Alto, CA, USA). Neurons labelled with Alexa Fluor 568 were confirmed by immunohistochemistry after recording.

Results

We sought to characterize translational abnormalities in the brains of LRRK2 mouse models, focusing on the caudate putamen, where substantia nigra dopamine neurons project to and is linked to the pathology of Parkinson's disease. To obtain high expression of G2019S LRRK2 or kinase dead G2019S/D1994A LRRK2 transgenes, we crossed mice harboring doxycycline-regulated LRRK2 expression constructs with the Ca^{2+}/calmodulin-dependent protein kinase II (CaMKII)-tTA driver mice (Lee et al., 2013; Xiong et al., 2017) . We then analyzed translation in the caudate putamen of the resulting G2019S LRRK2 or G2019S/D1994A LRRK2 transgenic mice, as well as LRRK2 knockout animals (Figure 1A, Figure 1-1, and Figure 1-2) (Nikonova et al., 2012).

We characterized translation by ribosome profiling, the deep sequencing of ribosome-protected mRNA fragments generated by nuclease digestion. Ribosome profiling provides a quantitative measurement of translation and reports on the precise location of translating ribosomes across the transcriptome (Ingolia et al., 2009). We inferred the

translational activity of different mRNAs by calculating the translation efficiency (TE), the ratio between the abundance of ribosome footprints derived from a gene to the overall abundance of its mRNA as determined by RNA-seq (Brar and Weissman, 2015; Ingolia, 2016). Comparison of the global distribution of TE values between LRRK2 transgenic mice and non-transgenic littermate control mice revealed broad alterations in TE distribution (Figure 1B). Likewise, LRRK2 knockout mice showed widespread differences in TE relative to wild-type control mice (Figure 1C). In contrast, G2019S/D1994A LRRK2 transgenic mice have a TE distribution similar to those in non-transgenic control mice, indicating that the changes in LRRK2 transgenic mice are dependent on kinase activity (Figure 1D) (Greggio et al., 2006; Smith et al., 2006). The broadly altered TE distribution indicates that G2019S LRRK2 causes increased expression of some genes (TE up) and decreased expression of others (TE down), distorting the overall translatome.

It has been shown that G2019S LRRK2 enhances the translation of transcripts containing complex 5'UTR structure (Kim et al., 2020). Therefore, we compared the predicted 5'UTR folding energy between genes showing elevated or reduced TE from each comparison. The TE up genes in G2019S LRRK2 transgenic mouse brain have significantly lower folding energy than randomly selected control genes with the same group size (Figure 2A), indicating that they have more complex 5'UTR secondary structures. Conversely, the TE down genes have significantly higher folding energy compared to the control genes, which suggests that they have less structured 5'UTR (Figure 2A). Notably, LRRK2 knockout mice show the reverse trend, indicating that loss

of LRRK2 has the opposite effect from hyperactive G2019S LRRK2 (Figure 2B). The same trend is clear when we stratify transcripts according to the strength of their 5'UTR secondary structure (Figures 2C and 2D). Unlike the case for 5'UTRs, 3'UTR folding energy does not show LRRK2-dependent correlation with TE (Figures 2-1, A and B). In addition, we did not find significant TE changes from 5' terminal oligopyrimidine (TOP)-containing genes, which are known to be regulated by phosphorylation of 4E-BP (Figures 2-1, C and D) (Thoreen et al., 2012). Therefore, our ribosome profiling data from the mouse brain samples indicate that LRRK2 enhances translation of mRNAs with complex 5'UTR secondary structure in a kinase activity-dependent manner.

Recent advances in molecular techniques that combine chemical probes and deep sequencing have provided transcriptome-wide measurements of RNA structure in living cells. We analyzed mouse RNA structure data (icSHAPE) (Spitale et al., 2015) to estimate basal levels of 5'UTR structural complexity of genes differentially regulated by LRRK2. Low icSHAPE signal indicates low chemical reactivity at a given nucleotide, thereby suggesting a higher likelihood that it participates in secondary structures in cells. We compared icSHAPE reactivity between TE up and TE down genes from G2019S LRRK2 transgenic and LRRK2 knockout mice. Structure probing data from 100nt windows 5' of the CDS start site revealed that the TE up genes in G2019S LRRK2 have significantly low average icSHAPE reactivity (0.229) associated with more complex structure, while the TE down genes have higher average reactivity (0.240) suggesting low structural complexity (Figure 2E). LRRK2 knockout mice show the opposite trend (up: 0.237, down: 0.219) (Figure 2F). These results suggest that the

5'UTR secondary structure adjacent to the start codon may play a role in the translatome alteration by G2019S LRRK2.

Translation initiation is a tightly regulated process, with many eukaryotic initiation factors (eIFs) involved in the regulation and facilitation of the process (Sonenberg and Hinnebusch, 2009; Jackson et al., 2010). Of note, DEAD-box RNA helicases including eIF4A, Ddx3, and Dhx29 are thought to resolve 5'UTR secondary structure of mRNAs with the help of other initiation factors such as eIF4B (Parsyan et al., 2011; Sen et al., 2015). Previous studies suggested that T136 phosphorylation of ribosomal protein S15 (uS19) mediates the translational effects of G2019S LRRK2 (Martin et al., 2014b; Kim et al., 2020). Consistent with this, we found that S15 T136 phosphorylation is increased in the G2019S LRRK2 transgenic mouse brain and decreased in the LRRK2 knockout mouse brain (Figures 3A and 3B). To investigate potential crosstalk between G2019S LRRK2, phosphorylated S15 and eIFs, we employed bicistronic reporters with hepatitis C virus (HCV) or cricket paralysis virus (CrPV) internal ribosome entry site (IRES). HCV- and CrPV-IRES do not require RNA helicase activity to initiate translation, and CrPV-IRES initiation is entirely independent of eIFs (Figures 3C and 3D) (Jackson et al., 2010). In these bicistronic reporter assays, cap-dependent translation of firefly luciferase is dependent on helicase activity of eIFs, while IRES-driven cap-independent translation of *Renilla* luciferase is helicase independent. Unexpectedly, both IRES reporters show the same cap-dependent and cap-independent translational induction by G2019S LRRK2 and T136D S15, thereby leaving the ratios between cap-dependent and cap-independent translation unchanged (Figures 3E to 3J and Figure 3-1). Since

401 the CrPV IRES does not require any initiation factors to recruit ribosomes, the results
402 indicate that the translational effects of G2019S LRRK2 are independent of translation
403 initiation factors, and phosphorylation of S15 is sufficient to enhance the translation of
404 mRNAs with structured 5' UTRs.
405
406 While we sought to characterize translational abnormalities in the LRRK2 knockout
407 mouse brain, we found unexpected patterns of ribosomal footprint distribution on the
408 *Atf4* upstream open reading frame (ORF) regions. *Atf4* is the key transcription factor
409 underlying one branch of the integrated stress response (ISR) pathway and its
410 expression is known to be translationally regulated (Vattem and Wek, 2004). eIF2α-
411 mediated regulation of *Atf4* is a well-studied example of translational regulation utilizing
412 termination-reinitiation balance between the upstream ORFs. We observed that in the
413 LRRK2 knockout brain, ribosome footprints are depleted 15 – 20 nucleotides prior to the
414 start codon of the main ORF (Figure 4A). We performed additional ribosome profiling
415 experiments with the caudate putamen (striatum, STR) and the ventral midbrain (VMB)
416 of LRRK2 knockout mouse brain and found that the footprint depletion is consistent
417 across all ribosome profiling experiments conducted (Figure 4B). Since we found that
418 5'UTR secondary structure is important to LRRK2-mediated translational regulation, we
419 examined potential secondary structures near the depleted region. Computational
420 secondary structure predictions (RNAfold) reported multiple potential hairpins in the *Atf4*
421 mRNA, and the depleted region in particular has a very high probability to form hairpin
422 (Figure 4C). These results further point to the importance of 5'UTR secondary structure
423 near start codon for the translational effects of LRRK2.

Since *Atf4* uORF footprint abnormality is observed in the LRRK2 knockout brain and *Atf4* induction is a central downstream pathway of ISR, we further sought to determine a potential relationship between G2019S LRRK2 and ISR. First, eIF2α phosphorylation levels in the G2019S LRRK2 transgenic brain were examined. We found no steady-state induction of eIF2α phosphorylation regardless of the transgene expression levels (Figure 4-1A). Next, we tested the potential relationship by inducing ISR in G2019S LRRK2-expressing primary neurons cultured from the transgenic mouse model. Of note, G2019S LRRK2-expressing neurons have defective recovery from thapsigargin-induced ISR (Figure 4-1B). Considering the enhanced translation of structured 5'UTR-containing transcripts in the G2019S LRRK2 brain, this defected recovery could be due to translational defects caused by G2019S LRRK2 inhibiting 5'UTR-mediated translational regulation required for ISR recovery. In addition, since thapsigargin induces ISR by blocking SERCA, defective calcium handling in G2019S LRRK2 neurons could also exacerbate ISR. A previous study suggested that dysregulated translation leads to increased calcium influx in G2019S LRRK2 human dopamine neurons (Kim et al., 2020). In this regard, we performed calcium recordings with the G2019S LRRK2 expressing brain. Basic electrophysiological properties including spontaneous and evoked action potential wave of substantia nigra pars compacta dopamine neurons are indifferent to G2019S LRRK2 expression in the brain (Figure 5-1). Substantia nigra dopamine neurons also show similar pacemaking activities compared to the wild-type (Figure 5A). However, calcium currents measurement showed significant increase of calcium currents in the G2019S LRRK2 expressing brain (Figures 5B and 5C). These

447 results are consistent with the previous report of increased calcium influx in G2019S
448 LRRK2 human dopamine neurons (Kim et al., 2020).
449
450 **Discussion**
451 In this study, we found that G2019S LRRK2 alters the global translational landscape in
452 the mouse brain. Dysregulated translation caused by G2019S LRRK2 has been
453 reported in Drosophila models and human dopamine neurons differentiated from
454 patient-derived iPSCs (Martin et al., 2014b; Kim et al., 2020). Our data from the mouse
455 brain are in line with the previous results showing that G2019S LRRK2 induces
456 genome-wide translational abnormality. In addition, the 5'UTR-mediated translational
457 shift, which was previously observed in the G2019S LRRK2 human dopamine neurons,
458 is also present in the mouse brain. In G2019S LRRK2 transgenic mice, mRNAs with
459 complex 5'UTR secondary structure tend to have elevated translation efficiency, while
460 LRRK2 knockout mice show the opposite trend. Analysis of RNA secondary structure
461 data suggest that mRNA secondary structure on the 5'UTR regions near the start codon
462 is important for these translation efficiency changes. These observations are in
463 accordance with the previous finding that G2019S LRRK2 alters genome-wide
464 translation by favoring mRNAs with complex 5'UTR secondary structure.
465
466 While the precise structural mechanism underlying the 5'UTR-mediated mRNA
467 preference is unclear, our IRES reporter assays suggest that the enhanced translation
468 in G2019S LRRK2 expressing neurons does not rely on translation initiation factors.
469 Considering that G2019S LRRK2 is known to phosphorylate multiple ribosomal proteins

including S15, our results bolster the idea that phosphorylation of ribosomal proteins could change the global translational landscape autonomously. Of note, the IRES reporter assays also indicate that the effects of LRRK2 may not be limited to translational initiation, since IRES-recruited ribosomes are thought to bypass scanning (Jackson et al., 2010). While our analyses indicate a strong correlation between 5'UTR secondary structure and translation efficiency, an alteration in secondary structure may in theory impact elongation as well. Secondary structure-mediated regulation is generally considered in the context of translation initiation since the coding region has limited degree of freedom for nucleotide-based secondary structure formation. However, as the *Atf4* CDS secondary structure prediction depicts, it is possible that elongation could be, at least partially, regulated by mRNA secondary structure as well. Therefore, these collectively suggest that the G2019S LRRK2 mutation and its downstream effects can facilitate translation during both initiation and elongation steps if secondary structure-mediated regulation is in place.

Ribosome footprint depletion at the *Atf4* 5'UTR in LRRK2 knockout provides new information on the mechanisms by which LRRK2 affects translation. It suggests that the low TE of complex 5'UTR genes in the LRRK2 knockout brain is due to strong hairpin formation and reduced ribosomal processivity. Alternatively, it is possible that the depletion is caused by disome formation, which can reduce the recovery of footprints in ribosome profiling experiments that include a monosome-specific size-selection step. This disome hypothesis is supported by the facts that the depletion is just in front of the main CDS start codon, and the main CDS also tends to form strong hairpin structure

493 right after the start codon (Figure 4C). Both cases are consistent with the interpretation
494 of reduced ribosomal processivity in the LRRK2 knockout brain. It further suggests that
495 uORF-mediated regulation of *Atf4* expression could potentially be regulated by
496 manipulating ribosomal processivity. While we did not find any *Atf4* footprint distribution
497 abnormality in the G2019S LRRK2 transgenic brain, we cannot exclude the possibility
498 that increased ribosomal processivity could impair the ISR, thereby incurring a long-
499 term cellular stress in G2019S LRRK2 PD. Delayed recovery from thapsigargin-
500 mediated ISR in G2019S LRRK2 neurons might be linked to this increased processivity.
501 Since ATF4 plays central roles in the integrated stress responses, including induction of
502 genes necessary to cope with cellular stresses, understanding the exact molecular
503 mechanisms for *Atf4* expression regulation will deepen our knowledge on the
504 pathobiology of LRRK2 PD.
505
506 Since this study was conducted with dissected brain tissues without cell-type specificity,
507 dopamine neuron-specific translational profiling experiments in rodent models, which
508 have been done in human iPSC-derived dopamine neuron and Drosophila models,
509 would further reveal the specific changes relevant to G2019S LRRK2 Parkinson's
510 disease (Kim et al., 2020; Pallos et al., 2021). In addition, there is a recent report
511 suggesting that G2019S LRRK2 leads to reduced bulk translation in rodent neurons
512 (Deshpande et al., 2020). The study was conducted with different model systems from
513 this study (cultured neurons, *in vitro* translation system, and skin fibroblasts), which
514 makes it hard to directly compare the results. However, bulk protein synthesis rate is
515 tightly related to the neuronal activity levels. In this regard, investigating the relationship

between LRRK2 and neuronal activity would be informative to collectively comprehend the molecular mechanisms of LRRK2-mediated translational regulation.

It is noteworthy that calcium influx is increased in the substantia nigra dopamine neurons in the G2019S LRRK2 expressing brain. The increased calcium influx was originally reported in G2019S LRRK2 human dopamine neurons. While the previous findings from cultured neurons initiated a plausible molecular mechanism that can led to a long-term dopamine neuronal stress, the electrophysiological characteristic of a neuron is heavily influenced by the neuron's wiring context. Therefore, monitoring calcium dynamics in a fully developed adult brain tissue is essential to validate the hypothesis (Yin et al., 2021). In this manner, our findings on the increased calcium influx *in vivo* bolster the suggested molecular etiology that calcium dysregulation leads to dopamine neuronal stress in the G2019S LRRK2 PD.

References

Anders S, Huber W (2010) Differential expression analysis for sequence count data. Genome Biol 11:R106.

Andres-Mateos E, Mejias R, Sasaki M, Li X, Lin BM, Biskup S, Zhang L, Banerjee R, Thomas B, Yang L, Liu G, Beal MF, Huso DL, Dawson TM, Dawson VL (2009) Unexpected lack of hypersensitivity in LRRK2 knock-out mice to MPTP (1-methyl-4-phenyl-1,2,3,6-tetrahydropyridine). J Neurosci 29:15846-15850.

Brar GA, Weissman JS (2015) Ribosome profiling reveals the what, when, where and how of protein synthesis. Nat Rev Mol Cell Biol 16:651-664.

539 Deshpande P, Flinkman D, Hong Y, Goltseva E, Siino V, Sun L, Peltonen S, Elo LL,
540 Kaasinen V, James P, Coffey ET (2020) Protein synthesis is suppressed in
541 sporadic and familial Parkinson's disease by LRRK2. FASEB J 34:14217-14233.
542 Gehrke S, Imai Y, Sokol N, Lu B (2010) Pathogenic LRRK2 negatively regulates
543 microRNA-mediated translational repression. Nature 466:637-641.
544 Greggio E, Jain S, Kingsbury A, Bandopadhyay R, Lewis P, Kaganovich A, van der
545 Brug MP, Beilina A, Blackinton J, Thomas KJ, Ahmad R, Miller DW, Kesavapany
546 S, Singleton A, Lees A, Harvey RJ, Harvey K, Cookson MR (2006) Kinase
547 activity is required for the toxic effects of mutant LRRK2/dardarin. Neurobiol Dis
548 23:329-341.
549 Imai Y, Gehrke S, Wang HQ, Takahashi R, Hasegawa K, Oota E, Lu B (2008)
550 Phosphorylation of 4E-BP by LRRK2 affects the maintenance of dopaminergic
551 neurons in Drosophila. EMBO J 27:2432-2443.
552 Ingolia NT (2016) Ribosome Footprint Profiling of Translation throughout the Genome.
553 Cell 165:22-33.
554 Ingolia NT, Ghaemmaghami S, Newman JR, Weissman JS (2009) Genome-wide
555 analysis in vivo of translation with nucleotide resolution using ribosome profiling.
556 Science 324:218-223.
557 Ingolia NT, Brar GA, Rouskin S, McGeachy AM, Weissman JS (2012) The ribosome
558 profiling strategy for monitoring translation in vivo by deep sequencing of
559 ribosome-protected mRNA fragments. Nat Protoc 7:1534-1550.
560 Jackson RJ, Hellen CU, Pestova TV (2010) The mechanism of eukaryotic translation
561 initiation and principles of its regulation. Nat Rev Mol Cell Biol 11:113-127.

562 Kim JW, Yin X, Jhaldiyal A, Khan MR, Martin I, Xie Z, Perez-Rosello T, Kumar M,
563 Abalde-Atristain L, Xu J, Chen L, Eacker SM, Surmeier DJ, Ingolia NT, Dawson
564 TM, Dawson VL (2020) Defects in mRNA Translation in LRRK2-Mutant hiPSC-
565 Derived Dopaminergic Neurons Lead to Dysregulated Calcium Homeostasis. Cell
566 Stem Cell 27:633-645.e637.
567 Lee Y, Karuppagounder SS, Shin JH, Lee YI, Ko HS, Swing D, Jiang H, Kang SU, Lee
568 BD, Kang HC, Kim D, Tessarollo L, Dawson VL, Dawson TM (2013) Parthanatos
569 mediates AIMP2-activated age-dependent dopaminergic neuronal loss. Nat
570 Neurosci 16:1392-1400.
571 Lorenz R, Bernhart SH, Honer Zu Siederdissen C, Tafer H, Flamm C, Stadler PF,
572 Hofacker IL (2011) ViennaRNA Package 2.0. Algorithms Mol Biol 6:26.
573 Martin I, Kim JW, Dawson VL, Dawson TM (2014a) LRRK2 pathobiology in Parkinson's
574 disease. J Neurochem 131:554-565.
575 Martin I, Kim JW, Lee BD, Kang HC, Xu JC, Jia H, Stankowski J, Kim MS, Zhong J,
576 Kumar M, Andrabi SA, Xiong Y, Dickson DW, Wszolek ZK, Pandey A, Dawson
577 TM, Dawson VL (2014b) Ribosomal protein s15 phosphorylation mediates
578 LRRK2 neurodegeneration in Parkinson's disease. Cell 157:472-485.
579 Nikonova EV, Xiong Y, Tanis KQ, Dawson VL, Vogel RL, Finney EM, Stone DJ,
580 Reynolds IJ, Kern JT, Dawson TM (2012) Transcriptional responses to loss or
581 gain of function of the leucine-rich repeat kinase 2 (LRRK2) gene uncover
582 biological processes modulated by LRRK2 activity. Hum Mol Genet 21:163-174.

583 Pallos J, Jeng S, McWeeney S, Martin I (2021) Dopamine neuron-specific LRRK2
584 G2019S effects on gene expression revealed by translatome profiling. Neurobiol
585 Dis 155:105390.
586 Parsyan A, Svitkin Y, Shahbazian D, Gkogkas C, Lasko P, Merrick WC, Sonenberg N
587 (2011) mRNA helicases: the tacticians of translational control. Nat Rev Mol Cell
588 Biol 12:235-245.
589 Sen ND, Zhou F, Ingolia NT, Hinnebusch AG (2015) Genome-wide analysis of
590 translational efficiency reveals distinct but overlapping functions of yeast DEAD-
591 box RNA helicases Ded1 and eIF4A. Genome Res 25:1196-1205.
592 Smith WW, Pei Z, Jiang H, Dawson VL, Dawson TM, Ross CA (2006) Kinase activity of
593 mutant LRRK2 mediates neuronal toxicity. Nat Neurosci 9:1231-1233.
594 Sonenberg N, Hinnebusch AG (2009) Regulation of translation initiation in eukaryotes:
595 mechanisms and biological targets. Cell 136:731-745.
596 Spitale RC, Flynn RA, Zhang QC, Crisalli P, Lee B, Jung JW, Kuchelmeister HY, Batista
597 PJ, Torre EA, Kool ET, Chang HY (2015) Structural imprints in vivo decode RNA
598 regulatory mechanisms. Nature 519:486-490.
599 Taymans JM, Nkiliza A, Chartier-Harlin MC (2015) Deregulation of protein translation
600 control, a potential game-changing hypothesis for Parkinson's disease
601 pathogenesis. Trends Mol Med 21:466-472.
602 Thoreen CC, Chantranupong L, Keys HR, Wang T, Gray NS, Sabatini DM (2012) A
603 unifying model for mTORC1-mediated regulation of mRNA translation. Nature
604 485:109-113.

605 Vattem KM, Wek RC (2004) Reinitiation involving upstream ORFs regulates ATF4
606 mRNA translation in mammalian cells. Proc Natl Acad Sci U S A 101:11269-
607 11274.
608 Xiong Y, Neifert S, Karuppagounder SS, Stankowski JN, Lee BD, Grima JC, Chen G,
609 Ko HS, Lee Y, Swing D, Tessarollo L, Dawson TM, Dawson VL (2017)
610 Overexpression of Parkinson's Disease-Associated Mutation LRRK2 G2019S in
611 Mouse Forebrain Induces Behavioral Deficits and alpha-Synuclein Pathology.
612 eNeuro 4.
613 Yin X, Kim JW, Liu S, Dawson TM, Dawson VL (2021) Protocol for measurement of
614 calcium dysregulation in human induced pluripotent stem cell-derived
615 dopaminergic neurons. STAR Protocols 2:100405.

616

617 **Legends**

618

619 **Figure 1. Broad alteration in mRNA translation in the G2019S LRRK2 mouse**
620 **brain.**
621 (**A**) A schematic of ribosome profiling workflow with mouse brain tissue. (**B** to **D**), TE
622 was calculated to estimate translational activity. Global TE distributions between (B) GS
623 LRRK2 TG and non-TG control, (C) LRRK2 KO and WT, (D) GS/DA LRRK2 TG and
624 non-TG control were compared. All values are in $\log_2$, and each data point represents a
625 single transcript. In scatterplots, centerline is a guideline with slope of 1, meaning that
626 the dots on the line do not have TE value differences between the genotypes. Standard
627 deviation of TE differences: 0.226 (GS LRRK2 vs control), 0.179 (GS/DA LRRK2 vs

628 control), 0.273 (LRRK2 KO vs WT). Standard z-score was calculated, and ±1.5 cut-off
629 was used to select TE up and TE down genes. Triplet periodicity is normal across the
630 results (Figure 1-1). (**E** and **F**) Histogram of TE differences (delta TE, ΔTE) between (E)
631 GS LRRK2 TG and non-TG control, or (F) LRRK2 KO and WT. Z-score ±1.5 cut-off was
632 used, and TE values are in $\log_2$. Each ribosome profiling experiment was firstly
633 analyzed independently to ensure reproducibility. Two independent results were
634 analyzed together by DESeq (Anders and Huber, 2010). (n=2). Expression analysis
635 results including TE values were compiled (Figure 1-2).
636
637 **Figure 1-1. Triple periodicity of ribosome profiling data.**
638 (**A** and **B**) Triplet periodicity of ribosome profiling datasets were visualized to ensure the
639 quality of the libraries. Transcript coordinates were re-aligned based on the rounded half
640 point of the ribosome footprint (5' end + (footprint length/2)). Conserved triplet
641 periodicity indicates that the libraries are faithfully representing translating ribosomes,
642 ensuring the quality of the RPF libraries. There was no significant change found in
643 ribosome footprint length, periodicity and distribution in any LRRK2 mouse models (data
644 not shown).
645
646 **Figure 1-2. Ribosome profiling expression analysis results.**
647
648 **Figure 2. 5'UTR secondary structure mediates translational effects of G2019S**
649 **LRRK2.**

(**A** and **B**) Correlation between estimated 5'UTR folding energy and translation efficiency changes in (A) GS LRRK2 TG, or (B) LRRK2 KO. Box plot overlaid with violin plot visualizes the median, the first and the third quartile along with the data distribution pattern. 5'UTR folding energy for transcripts was retrieved from UCSC genome database (mm9). The same z-score ±1.5 cut-off was used. Group sizes: GS TG (TE up: 687, TE down: 335), KO (TE up: 596, TE down: 576). Statistical significance was determined by one-way ANOVA with Bonferroni correction. (**C** and **D**) Genes with complex 5'UTR secondary structure (estimated folding energy: < -250kcal/mol, 1145 genes) or simple 5'UTR secondary structure (> -20kcal/mol, 1036 genes) were selected, and the TE differences between (C): GS LRRK2 TG mice and control mice (D): LRRK2 KO mice and WT mice were plotted. Statistical significance was tested with Wilcoxon signed-rank test ((C): $p < 0.001$ (Simple), $p = 0.03533$ (Complex); (D): $p = 0.6007$ (Simple), $p < 0.001$ (Complex). 3'UTR structures do not show correlation (Figure 2-1). (**E** and **F**) Differential icSHAPE reactivity profiles between TE up and TE down genes. The same TE up and TE down genes with z-score ± 1.5 were used; (E) GS TG (TE up: 687, TE down: 335), (F) LRRK2 KO (TE up: 596, TE down: 576). icSHAPE data from mouse ES cells were extracted (Spitale et al., 2015), and a window of -100 to 0 nucleotide 5' of start codon (CDS start) was used. Average icSHAPE reactivity values: all genes: 0.236, TE up (GS): 0.229, TE down (GS): 0.240, TE up (KO): 0.237, TE down (KO): 0.219. Statistical significance (compared to all genes) was measured by non-parametric Mann-Whitney test. Error bars indicate s.e.m. * $p<0.05$, ** $p<0.01$, *** $p<0.001$.

673 **Figure 2-1. 3'UTR secondary structure is not related to translational effects of**
674 **G2019S LRRK2.**
675 (**A** and **B**) 3'UTR secondary structure folding energy differences between TE up and TE
676 down genes (standard z-score ±1.5 was used). Unlike the 5'UTR folding energy
677 comparison, 3'UTR folding energy did not show opposing directions of effects between
678 G2019S (GS) LRRK2 transgenic (TG) and LRRK2 knockout (KO) mice. Statistical
679 significance was determined using Wilcoxon signed-rank test ((A): p = 0.002338 (TE
680 up), p = 0.02327 (TE down); (B): p = 0.01194 (TE up), p = 0.0254 (TE down)). (**C** and **D**)
681 TE differences of 5' TOP mRNAs in LRRK2 mouse models. Wilcoxon signed-rank test,
682 (C) p = 0.2112; (D) p = 0.09034. background signal. Error bars indicate s.e.m. * p<0.05,
683 ** p<0.01, ns = no significance.
684
685 **Figure 3. G2019S LRRK2 increases mRNA translation independent of initiation**
686 **factors.**
687 (**A** and **B**) Western blot and quantification of T136 S15 phosphorylation in the mouse
688 brain. (A) LRRK2 knockout (B) G2019S LRRK2 transgenic mice. Whole brain lysate
689 was used. n=3, biological replicates. Statistical significance was determined by (A)
690 unpaired t-test (B) one-way ANOVA with Bonferroni correction. (**C** and **D**) Schematics of
691 HCV- and CrPV-IRES reporters. (**E** to **G**) HCV-IRES reporter assays. (C): n=4, and (D):
692 n=3, respectively. (**H** to **J**) CrPV IRES reporter assays. (F): n=4 and (G): n=3,
693 respectively. Reporter assays were performed in primary mouse cortical neurons with
694 transient transfection, and each experiment is an average of triplicates. All values were
695 divided by the average of control values. Reporter mRNA levels were controlled (Figure

3-1). WT: wild-type. Fluc: firefly luciferase, RLuc: *Renilla* luciferase. RLU: relative light units. Statistical significance was determined by one-way ANOVA with Bonferroni correction. Error bars indicate s.e.m. * p<0.05, ** p<0.01, *** p<0.001, ns = no significance.

Figure 3-1. Reporter transcript levels for IRES reporter assays.

(**A** and **B**) qPCR measurement of luciferase transcript levels in IRES reporter assays. One-way ANOVA with Bonferroni correction was used, and there were no significant changes in the reporter transcript levels detected. ** p < 0.01, *** p < 0.001, ns = no significance.

Figure 4. Ribosome footprint distributions on Atf4 uORFs in the LRRK2 knockout brain.

(A and **B)** Ribosome footprints distribution in the 5'UTR of *Atf4* gene (visualized: chr15:80,086,569-80,086,862). Red box indicates the region that ribosomes are depleted in the LRRK2 knockout brain. (**C**) RNA structure prediction of the *Atf4* uORF sequences by ViennaRNA RNAfold (Lorenz et al., 2011). The regions of depleted ribosome footprints have high probability to form secondary structure. In addition, relationship between G2019S LRRK2 and eIF2α was addressed (Figure 4-1).

Figure 4-1. Delayed ISR recovery from G2019S LRRK2-expressing neurons.

(**A**) Phosphorylation of eIF2α in the G2019S LRRK2 transgenic brains. Dissected striatal tissues, age 3-4 months, n=3, biological replicates. (**B**) Mouse cortical neurons

were prepared from pregnant transgenic breeders at E15. Pups were separated and individually genotyped. Control: wild-type or single transgenic (CaMKII-tTA or tet-G2019S LRRK2), G2019S LRRK2: double transgenic. Tg: thapsigargin, 1μM). * background signal.

Figure 5. Calcium currents recorded in SNpc DA neurons.

(**A**) Comparison of spontaneous AP firing pattern of DA neurons between wild type and GS LRRK2 mouse slices. (**B**) Calcium currents were measured in mouse SNpc DA neurons using whole-cell patch clamp recordings. (**C**) Quantification of calcium peak currents. Data are expressed as means ± SEM, n = 12 slices from 12 animals for each group. Intrinsic properties were measured (Figure 5-1).

Figure 5-1. Intrinsic properties of mouse brain DA neurons.

(**A**) Summary of electrophysiological characteristics of DA neurons in SNpc during recordings, including pipette resistance (Rp), input resistance (Rin), series resistance (Rseries), leak currents (Leak), and resting membrane potential. (**B**) Spontaneous AP firing pattern in DA neurons. (**C**) A representative single AP wave with a half width of 2 ms. (**D**) Evoked APs. The presence of a sag (arrow) in the membrane potential and APs were detected in current-clamp immediately after rupturing the membrane. (**E**) Immunofluorescence image showing recorded neurons are tyrosine hydroxylase (TH)-positive. Alexa Fluor 568 was injected to label recorded neurons. Scale bar, 50 μm. Data are expressed as means ± SEM, WT, n = 6 slices from 6 mice; GS LRRK2, n = 6 slices from 6 mice.

745

746 **Figures**

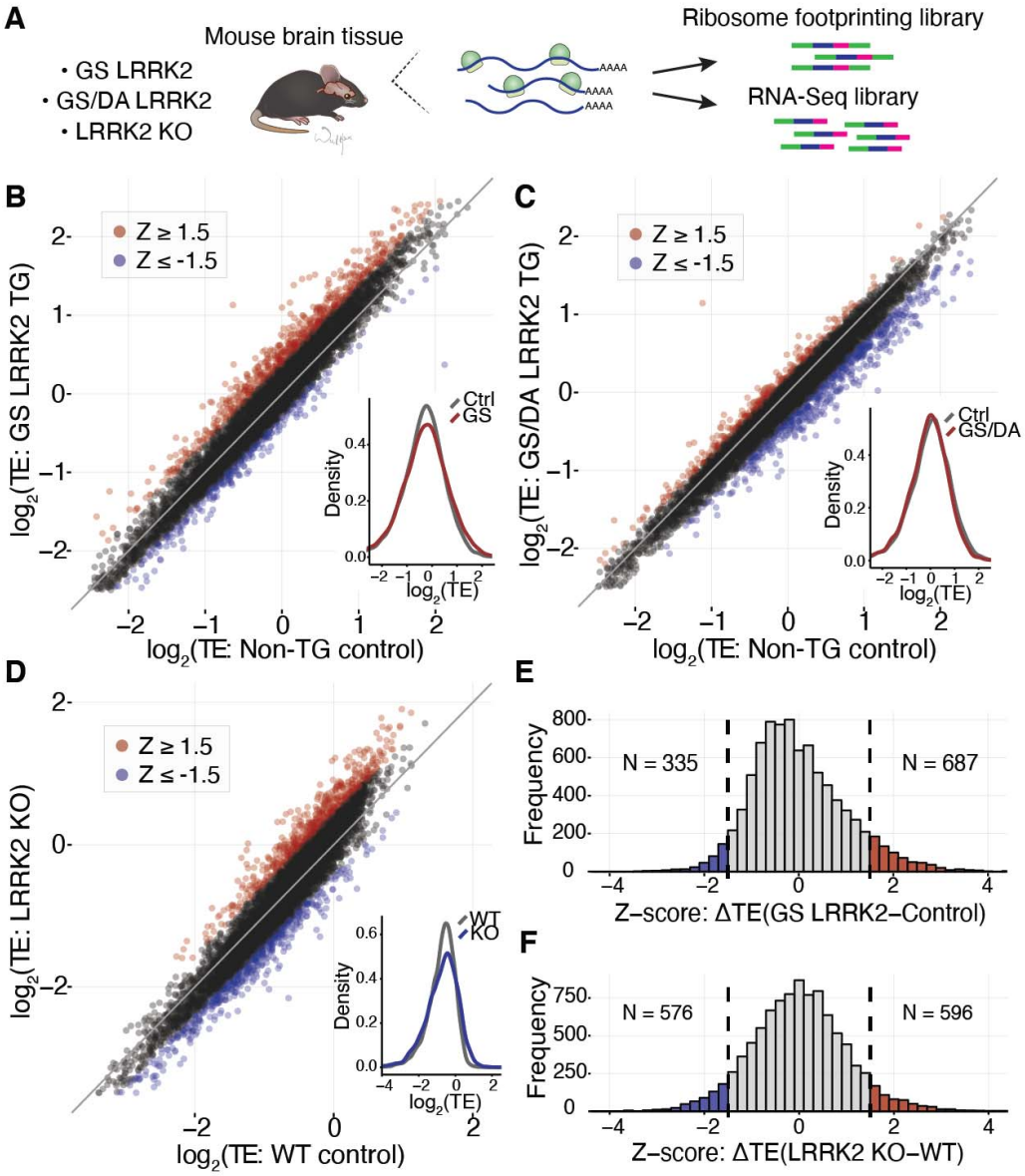

747

748 **Figure 1. Broad alteration in mRNA translation in the G2019S LRRK2 mouse**
749 **brain.**

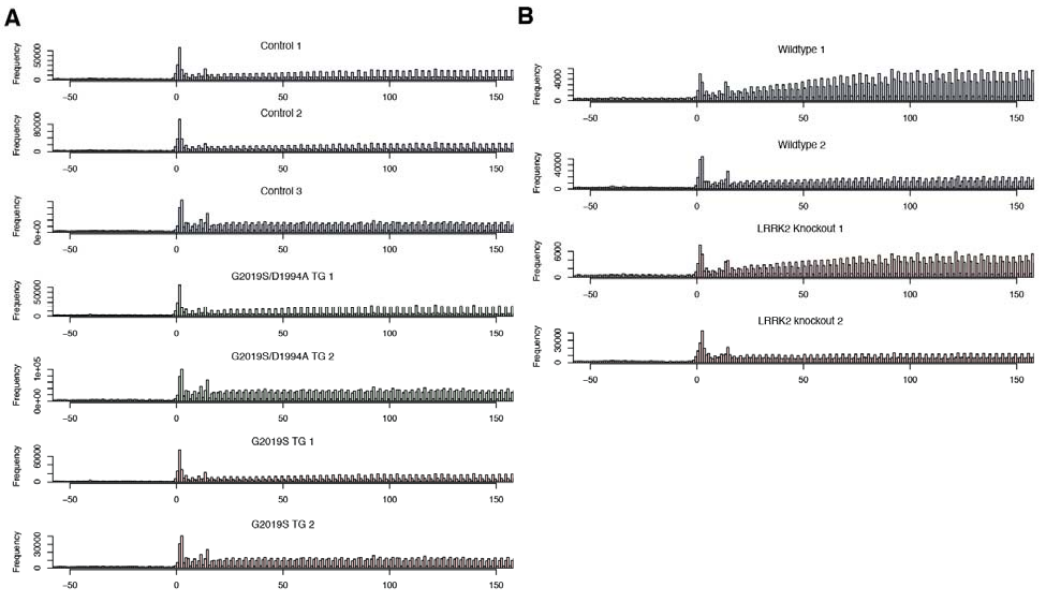

750
751 **Figure 1-1. Triple periodicity of ribosome profiling data.**

752

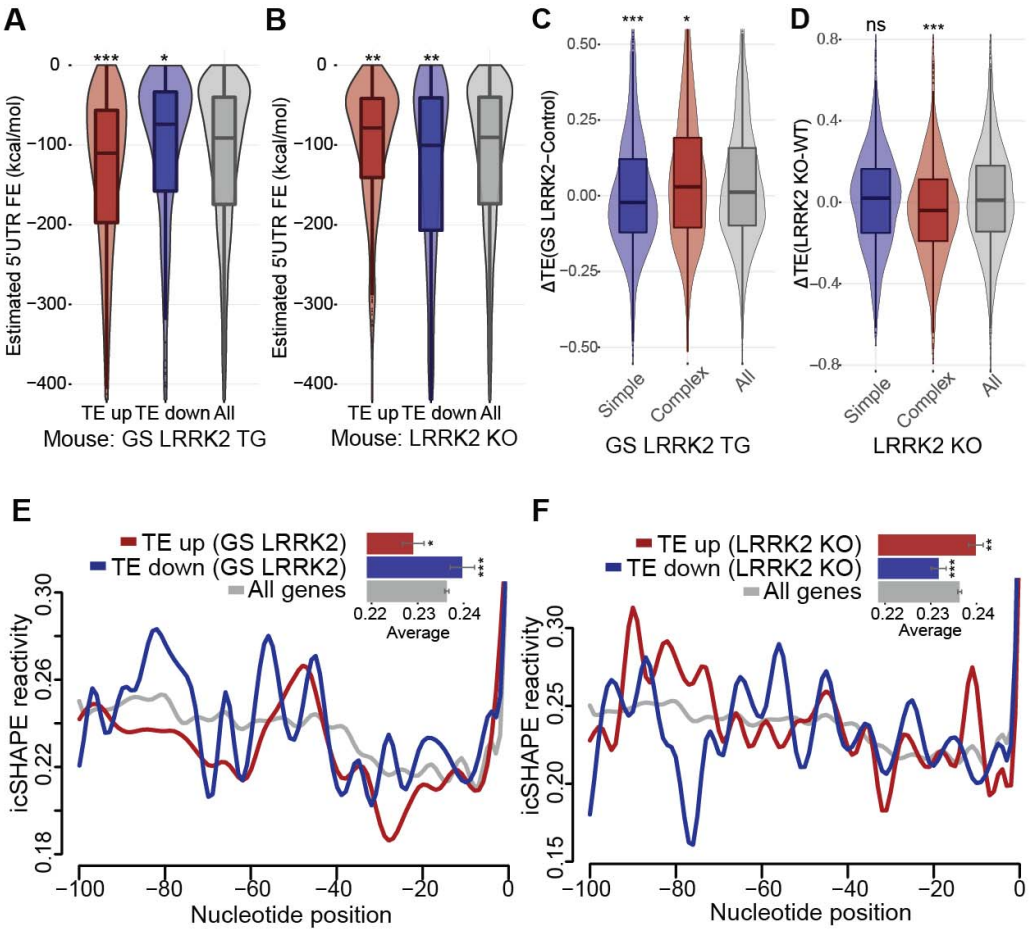

Figure 2. 5'UTR secondary structure mediates translational effects of G2019S LRRK2.

757

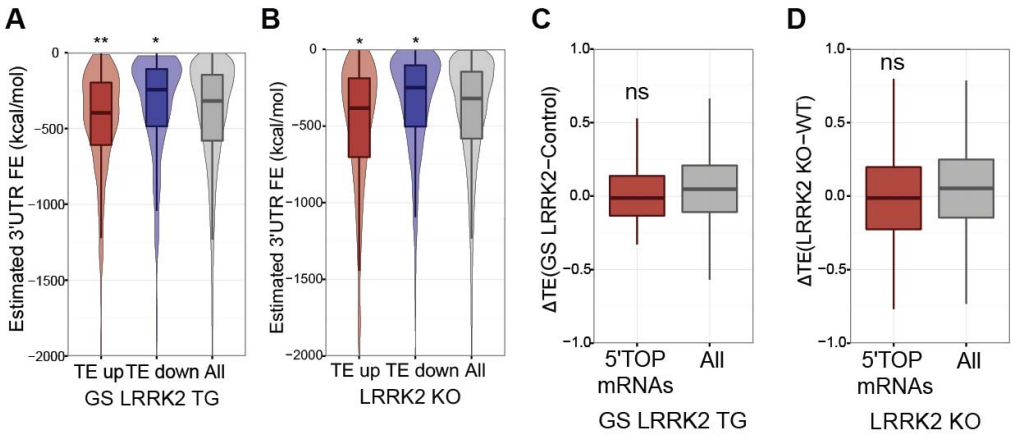

758

759 **Figure 2-1. 3'UTR secondary structure is not related to translational effects of**

760 **G2019S LRRK2.**

761

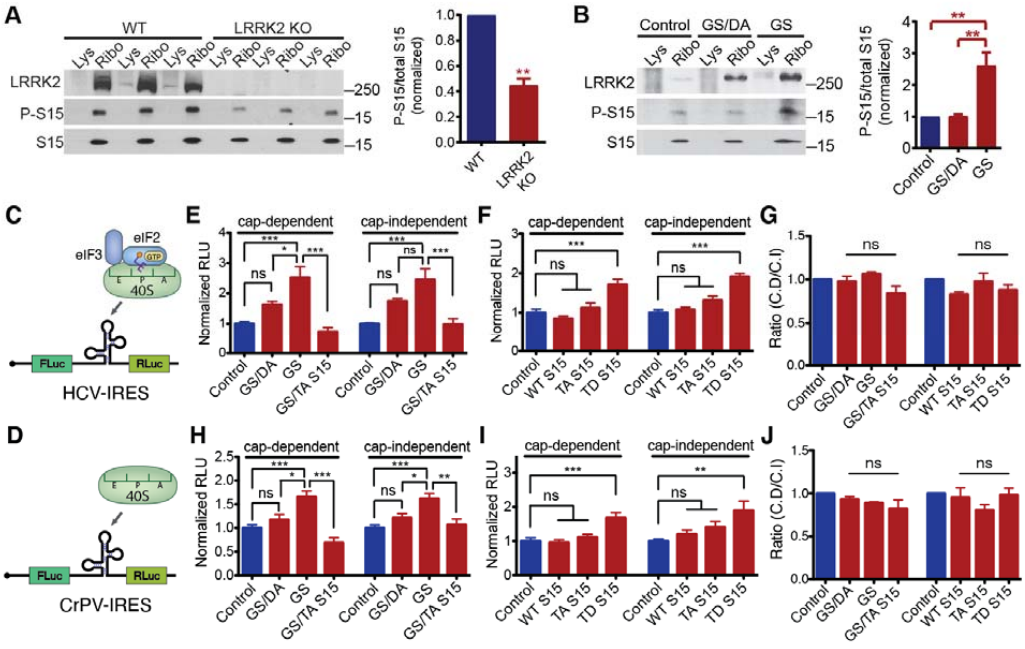

Figure 3. G2019S LRRK2 increases mRNA translation independent of initiation factors.

767

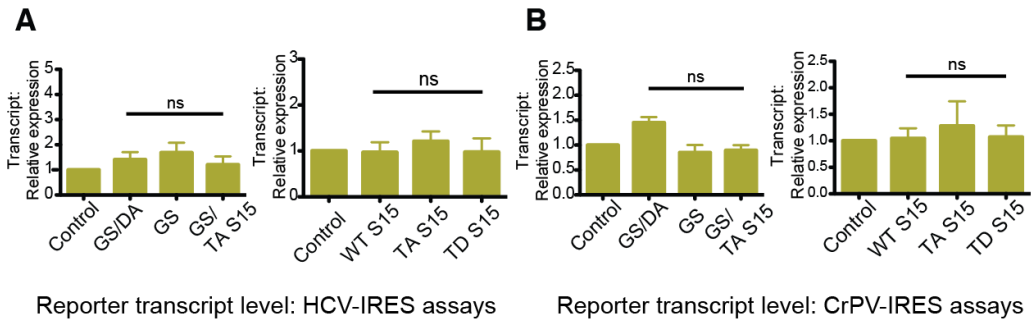

768
769

770 **Figure 3-1. Reporter transcript levels for IRES reporter assays.**

771
772

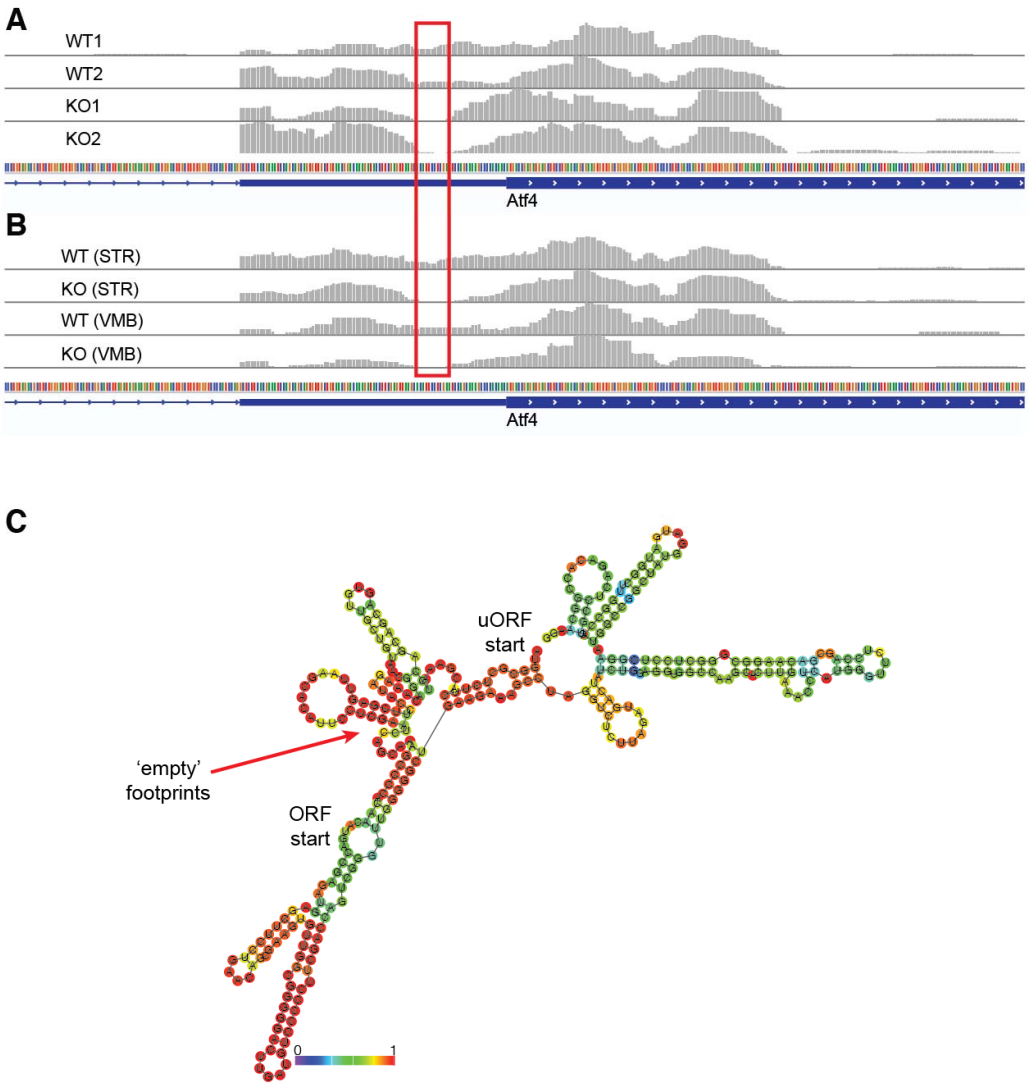

Figure 4. Ribosome footprint distributions on Atf4 uORFs in the LRRK2 knockout brain.

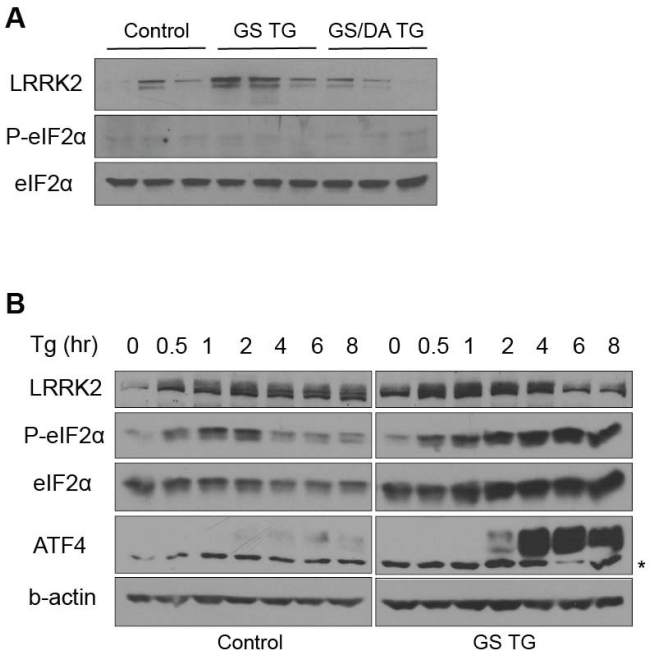

783
784

785 **Figure 4-1. Delayed ISR recovery from G2019S LRRK2-expressing neurons.**

786

787

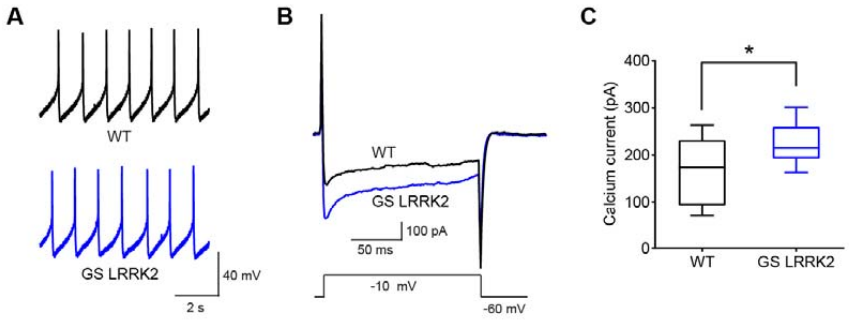

788
789
790 **Figure 5. Calcium currents recorded in SNpc DA neurons.**

791

792

A Summary of electrophysiological data

Feature	WT	TG
Rp (MΩ)	4.71 ± 0.56	4.68 ± 0.78
Rin (MΩ)	133.2 ± 14.9	129.7 ± 17.6
Rseries (MΩ)	21.71 ± 3.90	21.39 ± 3.51
Leak (pA)	-15.31 ± 3.52	-14.40 ± 2.24
Membrane potential (mV)	-62.8 ± 3.01	-63.5 ± 2.80

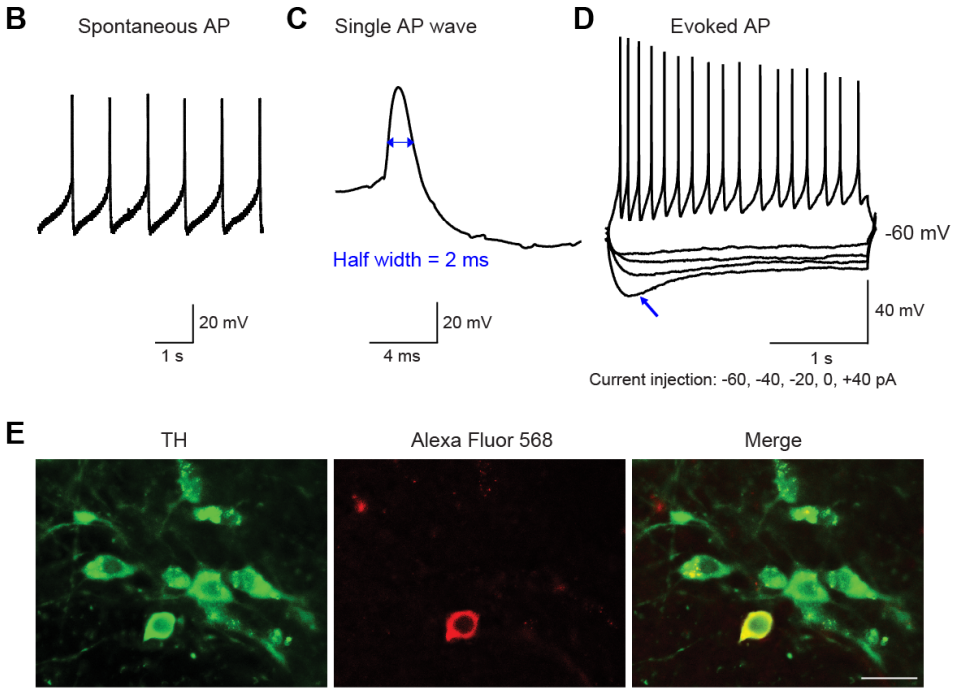

793
794

795 **Figure 5-1. Intrinsic properties of mouse brain DA neurons.**

796